ADVANCED FUNCTIONAL MATERIALS
www.afm-journal.de

Phase Reconstruction-Assisted Electron-Li^+ Reservoirs Enable High-Performance Li-S Battery Operation Across Wide Temperature Range

Yongqian He, Duanfeng Xiong, Yixin Luo, Wanqi Zhang, Sisi Liu, Yongjie Ye, Mengqing Wang, Ying Chen, Hong Liu, Jian Wang, Hongzhen Lin, Jincang Su,* Xianyou Wang, Hongbo Shu,* and Manfang Chen**

Lithium-sulfur batteries (LSBs) are known as high energy density, but their performance deteriorates sharply under high/low-temperature surroundings, due to the sluggish kinetics of sulfur redox conversion and Li^+ transport. Herein, a catalytic strategy of phase reconstruction with abundant "electron-Li^+" reservoirs has been proposed to simultaneously regulate electron and Li^+ exchange. As a demo, the 1T-phase lithiation molybdenum disulfide grown on hollow carbon nitride (1T-Li_xMoS_2/HC_3N_4) is achieved via in situ electrochemical modulation, where the 1T-Li_xMoS_2 serves as an auxiliary "Li^+ source" for facilitating Li^+ transport and the HC_3N_4 acts as an electron donor for electronic supplier. From the theoretical calculations, experimental and post-modern analyses, the relationship between the catalytic behaviors and mechanism of "electron-Li^+" reservoirs in accelerating the rate-determining kinetics of sulfur species are deeply understood. Consequently, the cells with 1T-Li_xMoS_2/HC_3N_4/PP functional separator demonstrate excellent long-term electrochemical performance and stabilize the areal capacity of 6 mAh cm^{-2} under 5.0 mg cm^{-2}. Even exposed to robust surroundings from high (60 °C) to low (0 °C) temperatures, the optimized cells exhibit high-capacity retention of 76.2% and 90.4% after 100 cycles, respectively, pointing out the potential application of catalysts with phase reconstruction-assisted "electron-Li^+" reservoirs in LSBs.

1. Introduction

With the consensus on global goals of "Carbon Peak" and "Carbon Neutrality", electrochemical energy storage systems are becoming increasingly popular.[1] In comparison to traditional lithium-ion batteries encountered with unsatisfactory energy density and high pollution, lithium-sulfur batteries (LSBs) have the advantages of high specific capacity (1675 mAh g^{-1}), environmental sustainability and low cost.[2] However, in addition to the challenges of lithium polysulfides (LiPSs) shuttling effect and the formation of Li dendrite,[3] the low redox conversion reaction kinetics of sulfur species directly contributes to the low discharge capacity and rapid capacity decay.[4] Reducing/increasing the surrounding temperature, the performance of LSBs will be even worse because of the deteriorating reaction kinetics/severe solvation and shuttling behavior.[5]

Toward addressing the low conductivity and sluggish electrochemical kinetics of

Y. He, Y. Luo, W. Zhang, S. Liu, Y. Ye, M. Wang, Y. Chen, H. Liu, X. Wang, H. Shu, M. Chen
National Base for International Science & Technology Cooperation of New Energy Equipment
Energy Storage Materials and Devices
National Local Joint Engineering Laboratory for Key Materials of New Energy Storage Battery
Hunan Province Key Laboratory of Electrochemical Energy Storage & Conversion
School of Chemistry
Xiangtan University
Xiangtan, Hunan 411105, China
E-mail: hongboshu@xtu.edu.cn; mfchen@xtu.edu.cn

The ORCID identification number(s) for the author(s) of this article can be found under https://doi.org/10.1002/adfm.202410899

DOI: 10.1002/adfm.202410899

D. Xiong, J. Su
School of Materials Science and Engineering
Xiangtan University
Xiangtan 411105, China
E-mail: sujc@xtu.edu.cn

J. Wang, H. Lin
i-Lab & CAS Key Laboratory of Nanophotonic Materials and Devices
Suzhou Institute of Nano-Tech and Nano-bionics
Chinese Academy of Sciences
Suzhou 215123, China
E-mail: jian.wang@kit.edu

J. Wang
Helmholtz Institute Ulm (HIU)
D89081 Ulm, Germany

J. Wang
Karlsruhe Institute of Technology (KIT)
D-76021 Karlsruhe, Germany

sulfur, the strategies of the electrical network and catalysis construcure are proposed to accelerate the electron and Li^+ migration ability, respectively.[6] In spite of conductive matrix, phase reconstruction of catalyst is also considered to be an effective strategy of regulating local electron density, resulting in the improvement of catalytic number, selectivity and activity.[7] For example, the layer-structured MoS_2 is initially investigated owing to the advantages of the feasible phase adjustment between 2H and 1T structure. Zhang et al.[8] systematically compared the difference of catalytic efficiency in propelling polysulfide conversions between 2H and 1T MoS_2 in LSBs, and discovered that 1T MoS_2 has the capability in promoting charge migration and accelerating sulfur reduction reactions (SRRs). However, the thermodynamic instability would cause the gradual phase transformation from 1T to 2H, resulting in the decrease and failure of catalytic activity.[9] Inserting smaller alkali metal atoms such as Li and Zn into the interlayer of 1T MoS_2 seems a better choice to reconstruct the electronic density to reduce its energy configuration.[10] Additionally, as known, the sulfur oxidation reactions (SORs) such as the delithiation process of Li_2S determine the re-utilization efficiency of sulfur species and has a significant impact on the rate of capacity decay of LSBs. To the best of our knowledge, the kinetic of the SORs process has been neglected in above works regarding catalysts, and there lacks the deep investigations on the catalytic mechanism.

As known, due to the slow migration kinetics and the slow desolvation process of Li^+, the kinetics of Li^+ formation and transport in the catalyst plays the decisive role in the utilization of sulfur species in the SRRs and SORs process.[11] For example, defect engineering[12] and single atom catalysis[13] are applied to further improve the mobility of Li^+ dissociated from $Li(solvents)_x^+$ or in the Li_2S interior. However, the kinetics of this process is limited by the $Li(solvents)_x^+$ concentration and higher energy barriers.[14] It is found that the 1T-Li_xMoS_2 constructed by inserting Li^+ into the 2H MoS_2 layer can act as a "Li^+ source" to contribute abundant Li^+ to the SRRs, further enhancing the ionic conductivity.[10b] In spite of Li^+ transport, the electron exchange around catalysts is also very important to the delithiation of Li_2S in the SORs process. Incorporating the "electron-Li^+" reservoirs into ideal catalyst is much of significance. This type of catalysts could not only as a pool to modulate Li^+ and electrons, but also kinetically and spontaneously accelerate the interconversions of sulfur species. Therefore, a comprehensive electronic and ionic diffusion modulation of catalyst should be considered to achieve the excellent performance of LSBs over the wide temperature range.

In this work, a catalytic strategy of employing abundant "electron-Li^+" reservoirs is proposed to accelerate the conversion kinetics of sulfur, even being exposed to the high- and low- temperature surroundings from 60 to 0 °C. In detail, the 1T-Li_xMoS_2 grown vertically on the hollow C_3N_4 (1T-Li_xMoS_2/HC_3N_4) is achieved by hydrothermal reaction and electrochemical reconstruction. The 1T-Li_xMoS_2 undergoing reconstruction could provide fast Li^+ transport, while the HC_3N_4 acts as the electron donor realizing electron-Li^+ mobility and adjusting the reservoir ability, which synergistically accelerates the conversion kinetics of SORs/SRRs. The combination of density functional theory (DFT) calculations, in situ UV and time of flight secondary ion mass spectrometry (TOF-SIMS) further successfully verify the role of 1T-Li_xMoS_2/HC_3N_4 in significantly improving the kinetics of SRRs and SORs. As a result, the cell with 1T-Li_xMoS_2/HC_3N_4/PP functional separator displays a capacity of 1668 mAh g^{-1} at 0.1 C and maintains high-capacity retention of 76.2%/90.4% after 100 cycles under high (60 °C)/low (0 °C) temperatures, respectively. Even under high-mass loading with 5 mg cm^{-2}, the cell exhibits an initial areal capacity of 6 mAh cm^{-2}. This work points out the way for potential application of "electron-Li^+" type catalysts in LSBs.

2. Results and Discussion

2.1. Simulation of "Electron-Li^+" Reservoir Structure on Adsorption and Delithiation Barriers

First of all, DFT calculations are adopted to assess the design of "electron-Li^+" reservoirs. The structures of 2H-MoS_2 (with trigonal prismatic coordination) and 1T-Li_xMoS_2 (with octahedral coordination) are depicted in **Figure 1a**. During the discharge process, when Li^+ intercalate into the van der Waals gaps between adjacent MoS_2 layers, they not only expand the interlayer spacing but also introduce additional electrons into the MoS_2 layers through charge transfer. This weakens the Mo-S *p-d* covalent interactions and reduces the stability of the crystal field, facilitating the transformation from the semiconducting 2H phase to the metallic 1T phase.[15] Specifically, the degeneracy and occupation of the Mo 4d orbitals differ between the 1T and 2H phases. In the stable semiconducting 2H phase, the $4d_{z^2}$ orbitals are fully occupied, while in the metastable metallic 1T phase, the $4d_{xy,\ yz,\ xz}$ orbitals are only partially occupied.[9] The insertion of Li^+ introduces extra electrons that half fill the $4d_{xy,\ yz,\ xz}$ orbitals, thereby enhancing the thermodynamic stability of the 1T phase. As shown in Figure 1b, the density of states (DOS) indicates the significantly notable difference near the fermi energy level between 1T-Li_xMoS_2 and 2H-MoS_2. Compared to 2H-MoS_2 of exhibiting semiconducting properties, 1T-Li_xMoS_2 exhibits a higher DOS, signifying stronger electron acceptor and typical metallic properties. The higher central distribution of the S-*p* band in 1T-Li_xMoS_2 by the projected density of state (PDOS) of the S-*p* energy band, suggesting a stronger hybridization with the Li-*s* band of LiPSs. Figure 1c delves into the band engineering influence of S-*p* band elevation on *s-p* hybridization. The elevation of the *p*-band centers in 1T-Li_xMoS_2 leads to the related elevation of the *s-p** (antibonding orbitals), resulting in a decrease in its electron acceptor capability, which produces a more stable molecules with stronger interactions. The inset of Figure 1c shows the adsorption behaviors with the corresponding differential charge density for Li_2S_6, highlighting the stronger interactions between 1T-Li_xMoS_2 and Li_2S_6. Then, in order to explore the functions on Li^+ migration, diffusion pathways on the substrate are simulated, and 1T-Li_xMoS_2 exhibits a lower Li^+ diffusion barrier compared to 2H-MoS_2 (0.18 vs 0.23 eV) (Figure 1d; Figure S1a, Supporting Information), further confirming its capability to accelerate Li^+ kinetics. Moreover, Ab Initio Molecular Dynamics (AIMD) simulation was performed to check the thermodynamic stability of 1T-Li_xMoS_2 structure. The results are shown in Figure S1b (Supporting Information), in which we can find that the total energy and temperature of the structure

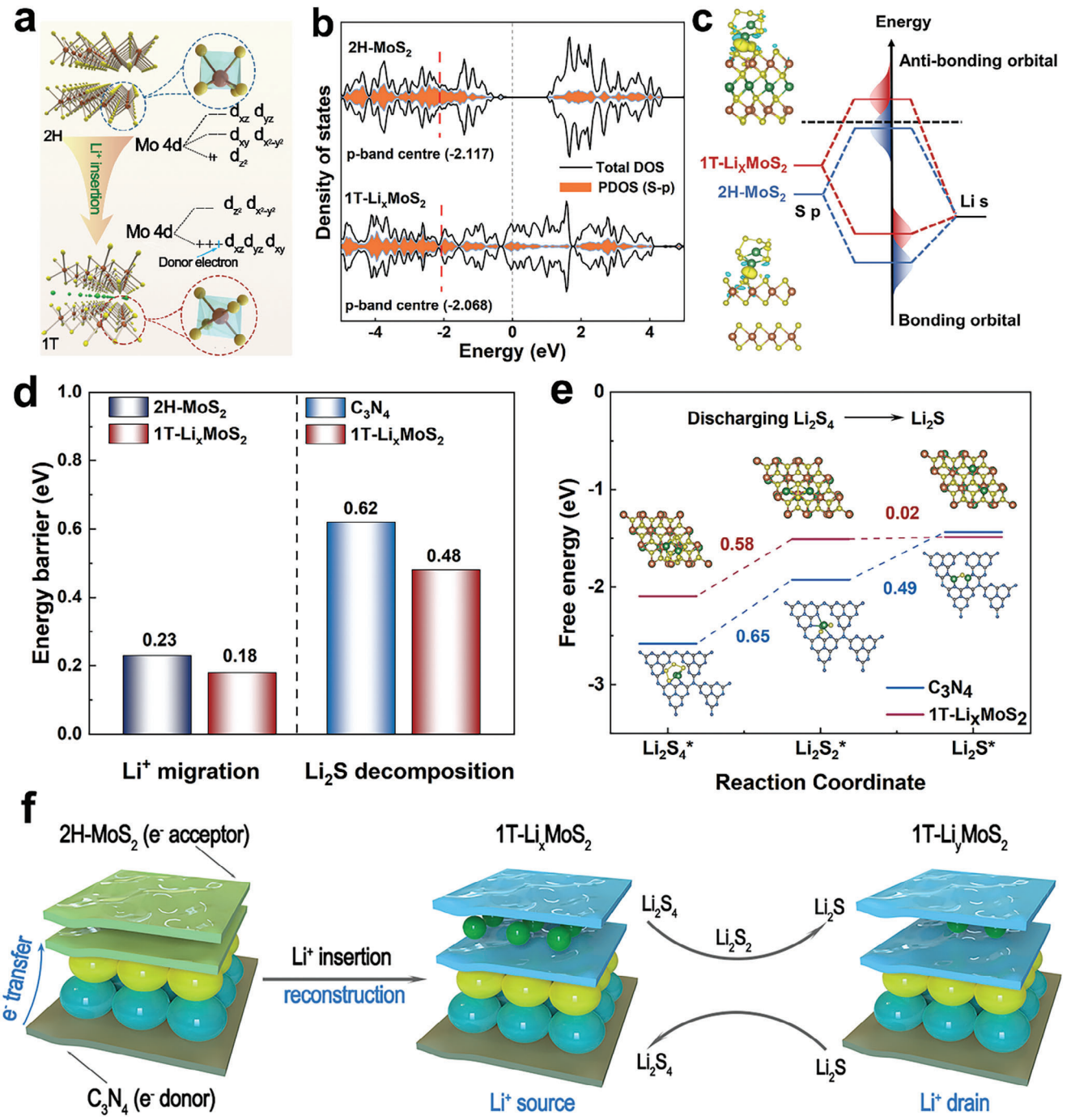

Figure 1. a) Schematic diagram of the phase reconstruction of MoS_2. b) DOS diagram. c) Band engineering influence of S-*p* band elevation on *s-p* hybridization. d) Comparison of Li^+ migration and Li_2S decomposition energy barriers, e) Free energy for sulfur species reduction. f) Modification mechanism diagram of "electron-Li^+" catalysts.

fluctuate very little around a fixed value during the simulation time. Furthermore, the structure 1T-Li_xMoS_2–Li_2S_8 remains intact during the simulation process, which confirms that 1T-Li_xMoS_2 is able to maintain a stable phase structure during electrochemical processes.

As known, the capacity is also related with the redox conversion kinetics of sulfur. Initially, the adsorption energies of sulfur species on MoS_2/HC_3N_4 and C_3N_4 were compared, and MoS_2/HC_3N_4 exhibited stronger interactions for all of the different species of sulfur species (Figure S1c, Supporting Information). Then, the Li_2S decomposition behavior in the SORs process is intimated via DFT calculations. As shown in Figure 1d and Figure S1d (Supporting Information), Li_2S on the 1T-Li_xMoS_2 has a lower delithiation barrier compared

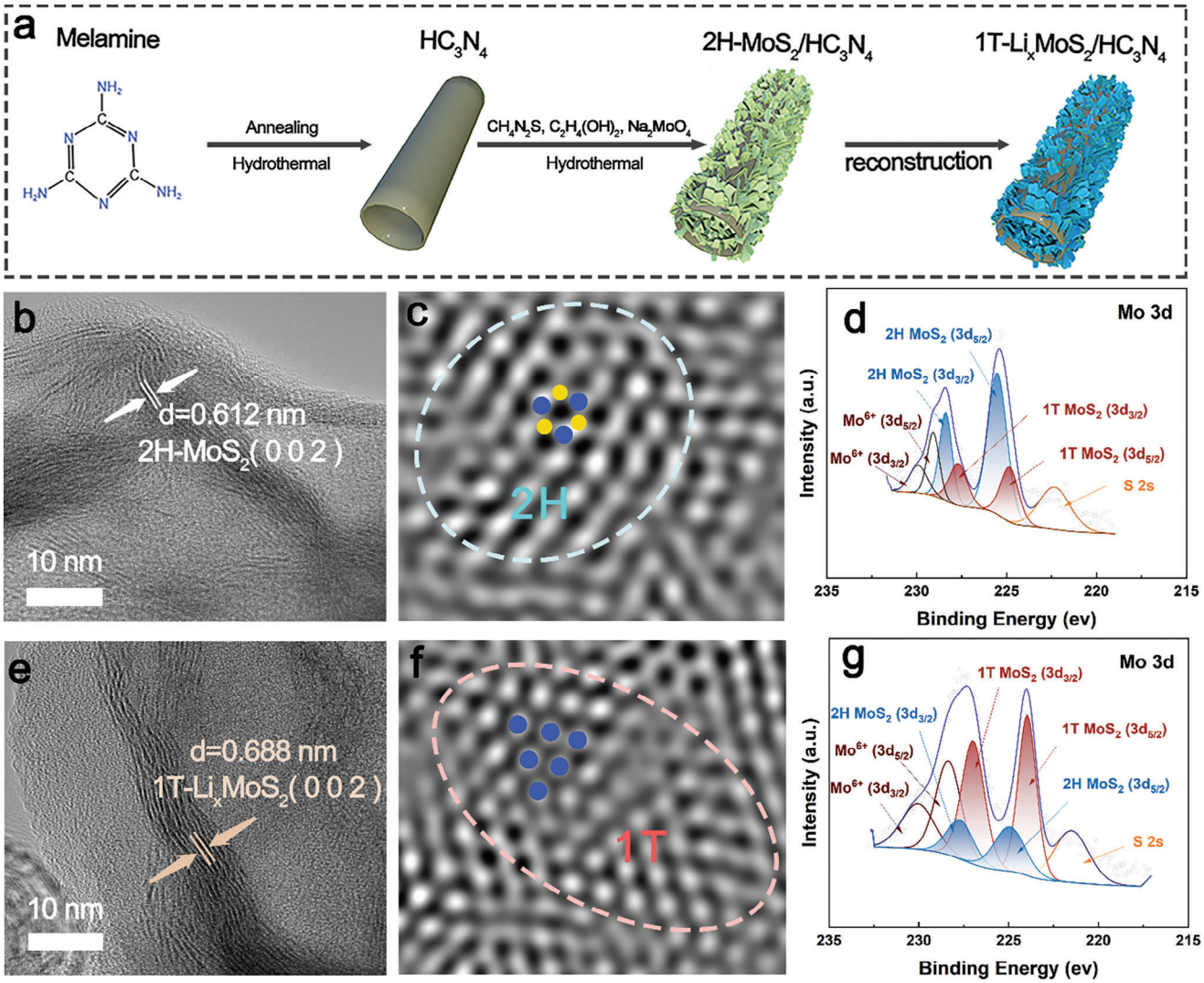

Figure 2. a) Material synthesis diagram. b,c) HRTEM images and d) XPS spectra of Mo 3d of 2H-MoS_2/HC_3N_4. e,f) HRTEM images and g) XPS spectra of Mo 3d of 1T-Li_xMoS_2/HC_3N_4.

to C_3N_4 (0.48 vs 0.62 eV), which is important for improving sulfur reutilization. The Gibbs free energies of $Li_2S_4 \rightarrow Li_2S_2$ and $Li_2S_2 \rightarrow Li_2S$, two key steps in SRRs, are then compared. Figure 1e shows that the free energy change of the liquid-solid conversion reaction is smaller under the help of 1T-Li_xMoS_2 and the successive solid-solid conversion reaction only accounts for 0.02 eV, highlighting its superior SRRs catalytic effect. Besides, the electrons in 1T-Li_xMoS_2/C_3N_4 will move directionally from the C_3N_4 side to the 1T-Li_xMoS_2 side (Figure S1e, Supporting Information), which implies that 1T-Li_xMoS_2 as an electron acceptor can promote the inserting of Li^+. Thus, 1T-Li_xMoS_2 acts as a "Li^+ source" to supply Li^+ to the SRRs, and also as a "Li^+ drain" to accept Li^+ from SORs through the electron-modulated action of C_3N_4 (Figure 1f). The combination of C_3N_4 with 1T-Li_xMoS_2 allows the optimization of electron-Li^+ transport, which further improves sulfur species utilization and guide the design of the "electron-Li^+" type electrocatalysts.

2.2. Synthesis and Related Characterizations of Phase-Reconstructed Electrocatalyst

Guided by above simulation, as illustrated in **Figure 2a**, the hydrothermal and electrochemical methods were adopted to fabricate ideal catalyst for the sulfur cathode. Briefly, the HC_3N_4 donor was initially synthesized. Subsequently, a hydrothermal reaction involving HC_3N_4, CH_4N_2S, $C_2H_4(OH)_2$, and Na_2MoO_4 yields vertically grown MoS_2 on the HC_3N_4 donor (2H-MoS_2/HC_3N_4). To investigate the optimal ratio of functional materials, functional separators with different metal contents were prepared, named 1T-Li_xMoS_2/HC_3N_4/PP-0.5, 1T-Li_xMoS_2/HC_3N_4/PP-1, and 1T-Li_xMoS_2/HC_3N_4/PP-1.5, respectively. Compared with the other two ratios of separators, the cell with 1T-Li_xMoS_2/HC_3N_4/PP-1 achieved both high capacity and high capacity retention (1513 mAh g^{-1}, 84.9%) (Figure S2, Supporting Information), suggesting that this ratio is optimal for the modification of Li-S batteries, and therefore 1T-Li_xMoS_2/HC_3N_4/PP-1 will be referred to as

1T-Li_xMoS_2/HC_3N_4/PP for simplicity. According to the TGA curves of 2H-MoS_2/HC_3N_4 under N_2 atmosphere, a stable plateau appeared when the temperature rises to 700 °C and the mass decreased by 60%, which can be attributed to the volatilization and decomposition of HC_3N_4 (Figure S3, Supporting Information). Therefore, the mass ratio of MoS_2 and HC_3N_4 is 2:3, which is consistent with the synthesis process. Furthermore, as shown in Figure S4a,b and Table S1 (Supporting Information), we prepared the separator with a functional layer thicknessr of 15.5–15.6 µm and the mass loading was 0.55–0.56 mg cm^{-2}. Meanwhile, the contact angle experiments between the separator and the electrolyte were also performed, and 1T-Li_xMoS_2/HC_3N_4/PP showed a stronger wettability compared to HC_3N_4/PP (8.9° vs 33.4°) (Figure S4c,d, Supporting Information), which represents a more adequate use of the active site. Furthermore, the morphology and phase changes were verified by transmission electron microscopy (TEM) and X-ray photoelectron spectroscopy (XPS). Nanoflower-like MoS_2 grows vertically on the HC_3N_4 surface and a lattice spacing of 0.612 nm is observed, corresponding to the (002) crystal plane of MoS_2 (Figure 2b; Figure S5a,b, Supporting Information).[16] The diffraction rings in selected area electron diffraction (SAED) is assigned to the (100) and (110) crystal planes of MoS_2 (Figure S5c, Supporting Information).[17] The crystal structure of MoS_2 is dominated by the 2H phase as shown by high-resolution TEM (HRTEM) in Figure 2c.[8] As shown in the XPS of Mo 3d, the 2H phase ($3d_{3/2}$ at 228.4 eV, $3d_{5/2}$ at 225.5 eV) and the 1T phase ($3d_{3/2}$ at 227.7 eV, $3d_{5/2}$ at 224.8 eV)[18] coexist in 2H-MoS_2/HC_3N_4, and the proportion of 2H phase substance is ≈68.78% (Figure 2d). After being activated by electrochemical method, the Li^+ insertion into the 2H-MoS_2/HC_3N_4 and the 2H-MoS_2 is converted into the 1T-Li_xMoS_2, leading to the phase reconstruction and formation of 1T-Li_xMoS_2/HC_3N_4 as confirmed by TEM (Figure S5d, Supporting Information). In the HRTEM, the lattice spacing of the (002) crystal plane of MoS_2 is increased from 0.612 to 0.688 nm, showcasing the success of Li^+ insertion (Figure 2e; Figure S5e, Supporting Information). Furthermore, the Energy dispersive spectrometer (EDS) demonstrated that the N, C, S, and Mo elements are well-distributed in 1T-Li_xMoS_2/HC_3N_4 (Figure S5f, Supporting Information). In comparison with original crystalline, the crystal structure has changed to be dominated by the 1T phase after lithiation (Figure 2f).[8] Also observed was a shift in the XPS peak of Mo 3d, and the proportion of 1T phase has been changed to ≈69.49% (Figure 2g). Besides, the X-ray diffraction (XRD) pattern shows that the peak corresponding to the (002) crystal planes[19] of 1T-Li_xMoS_2/HC_3N_4 are shifted to a lower angle and new diffraction peaks appear at ≈9° (2θ) (Figure S5g, Supporting Information), which suggests the expansion of the layer spacing and the reconfiguration of the crystal structure. Further combined with the Raman spectra, as shown in Figure S5h (Supporting Information), the characteristic peak situated at ≈700 cm^{-1} is attributed to the N-symmetric stretching of s-triazine ring.[20] Besides, the two characteristic peaks centered at 384.7 and 406.2 cm^{-1} can be ascribed to the $E_{2g}{}^1$ and A_{1g} vibration modes of MoS_2, respectively.[21] In addition, compared to 2H-MoS_2/HC_3N_4, the characteristic peaks at 148.7, 223.7, and 332.7 cm^{-1} (known as J_1, J_2, and J_3)[3] of 1T-Li_xMoS_2/HC_3N_4 are significantly enhanced, suggesting a phase transformation of MoS_2 from 2H to 1T. These results successfully confirmed the presence of "electron-Li^+" reservoirs via phase reconstruction method.

2.3. Electrochemical Electron-Li^+ Transport Kinetics on SRRs/SORs

The catalytic effects of 1T-Li_xMoS_2/HC_3N_4 was evaluated by various electrochemical measurements of Li^+ transport and polysulfide redox conversion. The distribution of relaxation time (DRT) method is adopted to fit electrochemical impedance spectrum (EIS), which can provide a more intuitive and realistic depiction of impedance spectra changes for each part.[22] **Figure 3a,b** shows the DRT evolution before and after cycling, and it can be observed that the Li^+ diffusion resistance (low frequency region)[23] dominates the overall resistance of the cell. Notably, the cell with 1T-Li_xMoS_2/HC_3N_4/PP shows a much lower Li^+ diffusion resistance in comparison to that with HC_3N_4/PP (28.9 vs 784.3 Ω). The LiPSs and Li^+ diffusion resistances of 1T-Li_xMoS_2/HC_3N_4/PP remain lower after cycling (5.9 and 81.8 Ω), which indicates a more complete conversion of LiPSs. Then, the galvanostatic intermittent titration technique (GITT) is used to observe the kinetic processes of the cells. The conversion efficiency between liquid-solid sulfur species determines the overall kinetics of the cell, and the cell with 1T-Li_xMoS_2/HC_3N_4/PP displays a lower difference of potential (51 and 137 mV) compared to that with HC_3N_4/PP (64 and 151 mV) (Figure S6a,b, Supporting Information). Furthermore, based on the Li^+ diffusion coefficients and internal resistance calculated using the GITT technique could provide deeper insights into the storage and transport mechanisms of Li^+ within electrode materials. The calculations reveal that, compared to batteries with HC_3N_4/PP, the batteries incorporating 1T-Li_xMoS_2/HC_3N_4/PP exhibit a more stable and higher Li^+ diffusion coefficient (−12.3 vs −11.6) as well as smaller Li_2S nucleation and activation internal resistances during charging and discharging cycles. This observation validates the concept that 1T-Li_xMoS_2/HC_3N_4 acts as the Li^+ reservoir, accelerating the transport of Li^+ (Figure S6a–d, Supporting Information). The accelerated kinetics is also reflected in the precipitation and dissolution of Li_2S during the redox processes.[24] For HC_3N_4, a notable transition occurs after 3 000 s. Specifically, the precipitation of Li_2S gradually tapers off, and the reduction of Li_2S_6 gradually become the predominant process. This transition is attributed to the formation of a Li_2S layer on the surface of the HC_3N_4 catalyst. The formation of this Li_2S layer acts as a physical and electrochemical barrier, significantly reducing the catalytic efficiency of the HC_3N_4 surface, resulting in a capacity of only 73.7 mAh g^{-1}. In contrast, the capacity of 1T-Li_xMoS_2/HC_3N_4 reaches 224.5 mAh g^{-1}, highlighting its superior catalytic capacity in Li_2S precipitation (Figure 3c; Figure S7a, Supporting Information). Further exploration into the growth patterns of Li_2S precipitation is conducted through peak fitting,[25] and the cell with 1T-Li_xMoS_2/HC_3N_4 exhibits a 3D nucleation growth pattern, which allows for a significant improvement in the utilization of active materials and catalytic sites (Figure S7b, Supporting Information). In the Li_2S dissolution experiments, the weak electron conductivity of HC_3N_4 makes it difficult to maintain the SORs. In contrast, 1T-Li_xMoS_2/HC_3N_4 exhibits excellent SORs catalysis (29.8 vs 437.2 mAh g^{-1}) (Figure S7c,d, Supporting

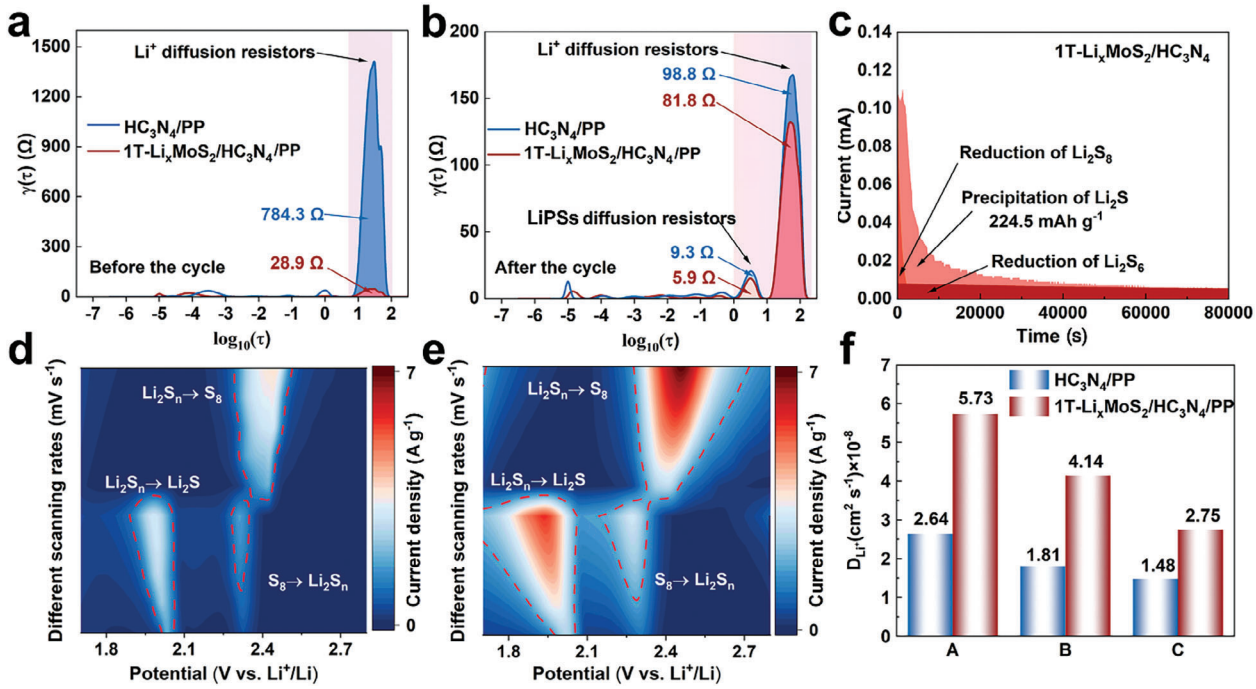

Figure 3. a,b) DRT. c) Profile of precipitation of Li_2S of 1T-Li_xMoS_2/HC_3N_4. Contour plots of CV patterns for d) HC_3N_4/PP and e) 1T-Li_xMoS_2/HC_3N_4/PP. f) Li^+ migration coefficients.

Information), and this efficient catalytic activity stems from the fast electron-Li^+ transport together with the phase reconstruction of the functional material. Moreover, 1T-Li_xMoS_2/HC_3N_4/PP has a lower shuttling current (0.001 mA) compared to HC_3N_4/PP (0.002 mA), indicating its more effective inhibition of the shuttle effect (Figure S8, Supporting Information).

Later, the relationship between electrochemical kinetics and catalytic capacity is verified by the cyclic voltammetry (CV) tests, the cell with 1T-Li_xMoS_2/HC_3N_4/PP has higher response currents in both the reduction ($S_8 \rightarrow Li_2S_n$, $Li_2S_n \rightarrow Li_2S$) and oxidation ($Li_2S_n \rightarrow S_8$) processes of the sulfur species than that with HC_3N_4/PP, exhibiting excellent catalytic performance (Figure 3d,e; Figure S9a,b, Supporting Information). By fitting, 1T-Li_xMoS_2/HC_3N_4/PP demonstrates faster Li^+ migration rates on peaks A, B, and C, which confirms the superior Li^+ conductivity (Figure 3f; Figure S9c and Table S2 and Equation S1, Supporting Information). Comparing the CV curves at 0.1 mV s^{-1}, 1T-Li_xMoS_2/HC_3N_4/PP exhibits a lower chemical double-layer capacitance (C_{dl}) (9.94 vs 2.65 mF cm^{-2}) and a lower Tafel slope (Figure S10a–f, Supporting Information), which demonstrates the advantages of 1T-Li_xMoS_2/HC_3N_4 in increasing the electrochemically active surface area and improving the kinetics of LSBs, displaying the promotion of 1T-Li_xMoS_2/HC_3N_4 for electrochemical kinetics and electron-Li^+ transport kinetics.

2.4. Robust Capacity and Long-Term Life Achieved by "Electron-Li^+" Reservoirs

Further, the charge/discharge and cycling performance of the cells were evaluated under various conditions. In the rate test, the cell with 1T-Li_xMoS_2/HC_3N_4/PP consistently exhibits higher initial capacity and stability, notably with an initial discharge specific capacity reaching a remarkable 1668 mAh g^{-1} at 0.1C (**Figure** 4a). In the galvanostatic charge/discharge (GCD) curves under different rates, 1T-Li_xMoS_2/HC_3N_4/PP shows additional capacity during charging, which is not part of the oxidation of Li_2S (highlighted by the pink rectangle) (Figure 4b; Figure S11a, Supporting Information). Therefore, the additional capacity of the 1T-Li_xMoS_2/HC_3N_4/PP cell without sulfur cathode is tested, which shows a consistent capacity of over 80 mAh g^{-1} even after 500 cycles at 0.1C, supporting the capability in "Li^+ source" and "Li^+ drain" (Figure S11b,c, Supporting Information). Then, the GCD profiles of 1T-Li_xMoS_2/HC_3N_4/PP has lower overpotential and lower potential barriers for Li_2S dissolution and nucleation than HC_3N_4/PP at 0.1 C, which indicates that it has excellent reversibility in the cycling process (Figure S12a–d, Supporting Information). Besides, 1T-Li_xMoS_2/HC_3N_4/PP also exhibits a lower capacity degradation ratio compared to HC_3N_4/PP after 72 h of shelving (8% vs 19%), reflecting its excellent resistance to self-discharge in inhibiting LiPSs shuttling (Figure 4c; Figure S13, Supporting Information). To test the cycling performance of the batteries, as shown in Figure S14 (Supporting Information), after 100 cycles at 0.2C, the discharge specific capacity of the battery with 1T-Li_xMoS_2/HC_3N_4/PP is much higher than that of the battery with HC_3N_4/PP (1285 vs 582 mAh g^{-1}). Then, the surface morphology of Li anodes after 100 cycles at 0.2C was monitored by SEM. A large number of Li dendrites was observed on the surface of the Li anode of the HC_3N_4/PP cell (Figure S15a, Supporting Information). In contrast, the surface of the Li anode of the 1T-Li_xMoS_2/HC_3N_4/PP cell was relatively smooth, confirming the uniform deposition of Li^+ (Figure S15b,

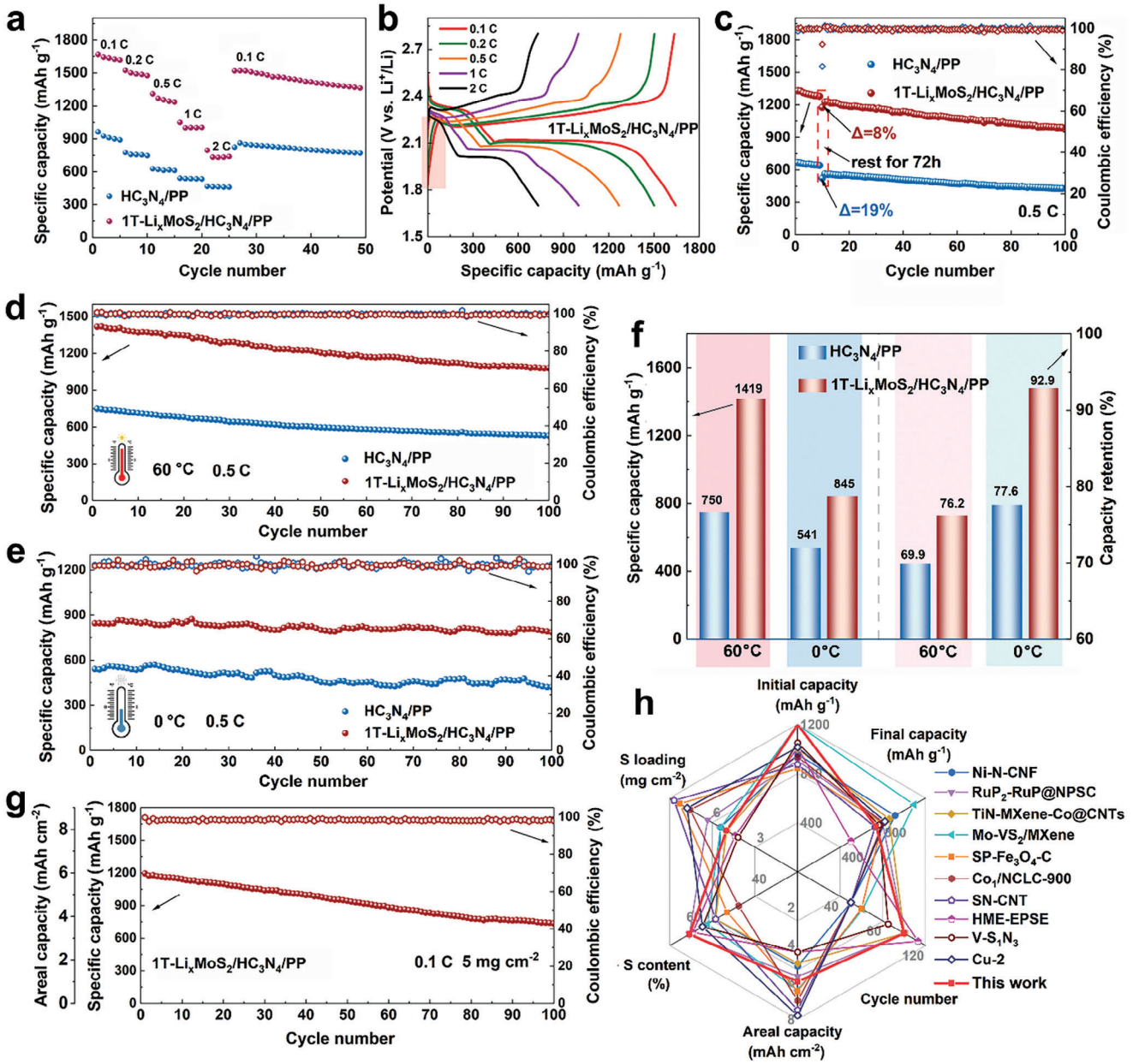

Figure 4. a) Rate performance and b) GCD curves. c) Self-discharge performance at 0.5C. Cycling performance at 0.5C under d) 60 °C and e) 0 °C. f) Comparison of initial capacity and capacity retention at 60 and 0 °C temperatures. g) Cycling performance with a S loading of 5 mg cm^{-2} and h) Comparison of performance parameters with recent works.

Supporting Information). This observation strongly suggests that 1T-Li_xMoS_2/HC_3N_4/PP is able to effectively regulate the Li^+ transport, thus avoiding the formation of Li dendrites and the polysulfide shuttling that could affect the performance of the cells. Further, to test the cycling performance of 1T-Li_xMoS_2/HC_3N_4/PP in LSBs at high current densities, the discharge specific capacity still reaches 570 mAh g^{-1} and the coulombic efficiency is still as high as 99.7% after 400 cycles at 3C, exhibiting excellent cycling stability (Figure S16, Supporting Information).

Further, cycling performance under different temperature conditions is investigated.[5] Increasing the temperature would accelerate the reaction kinetics and cause the severe LiPSs shuttling as well. As exhibited in Figure 4d, under 60 °C, the cell with 1T-Li_xMoS_2/HC_3N_4/PP shows an initial specific capacity of 1419 mAh g^{-1} at 0.5C and a capacity retention rate is 76.2% after 100 cycles, which is higher than that with HC_3N_4/PP (750 mAh g^{-1} and 69.9%). When the temperature is reduced to 0 °C, the diffusion kinetics of Li^+ and the dissolution kinetics of Li_2S may be the key issue. The 1T-Li_xMoS_2/HC_3N_4/PP still exhibits an advantage in capacity and retention over HC_3N_4/PP (827 mAh g^{-1}, 90.4% vs 541 mAh g^{-1}, 77.6%) (Figure 4e). As summarized in Figure 4f, the increased capacity retention strongly demonstrates excellent wide temperature adaptability. To further explore the

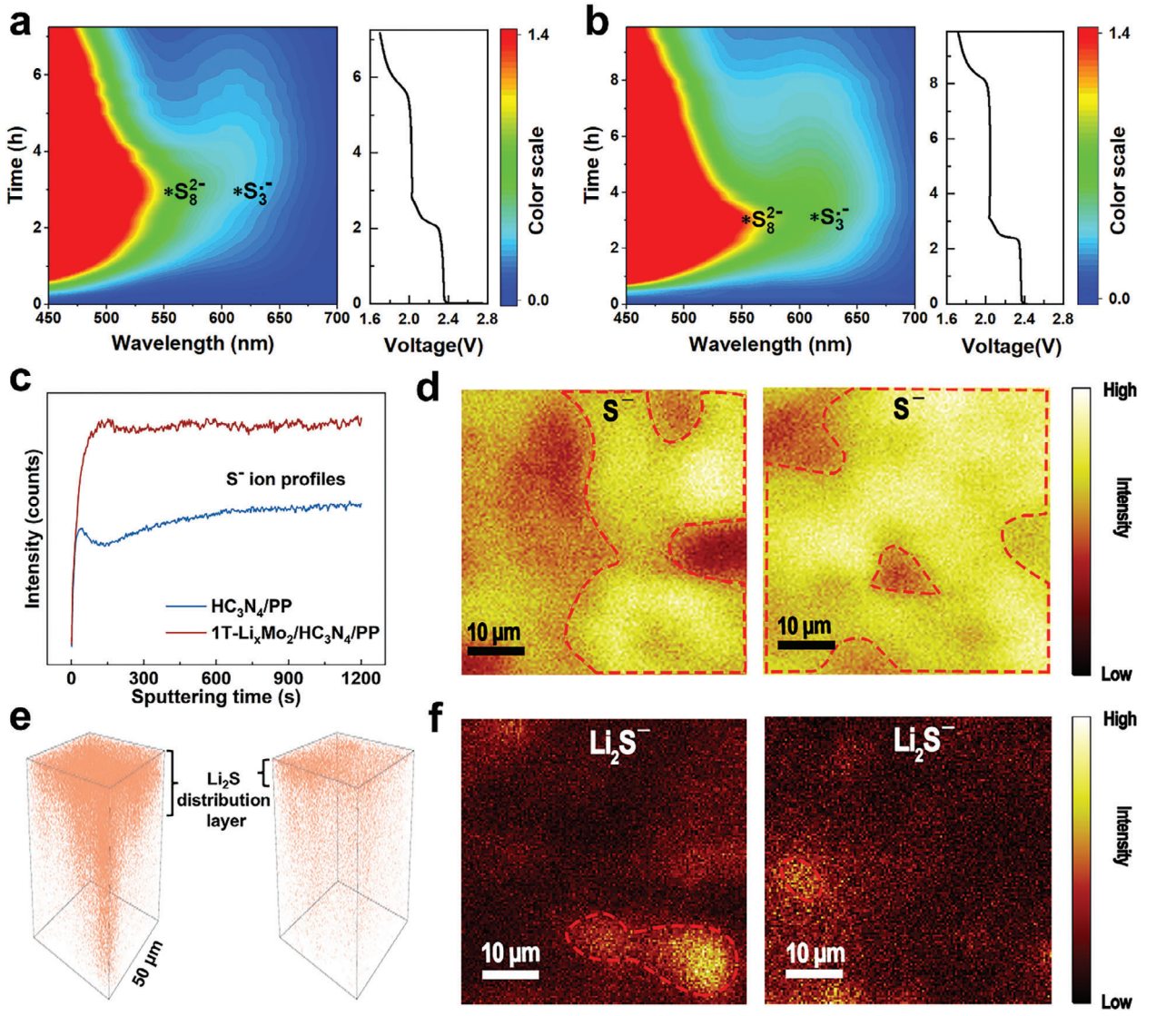

Figure 5. The in situ UV for a) HC_3N_4 and b) 1T-LixMoS$_2$/HC_3N_4. c) TOF-SIMS S^- ion depth profiles of S cathode after operating for 20 cycles and d) mappings on the top surface. e) TOF-SIMS 3D rendering Li_2S depth profile image of Li anode, f) mappings on the top surface of Li anode surface (HC_3N_4 on the left, 1T-Li_xMoS_2/HC_3N_4 on the right).

effectiveness of the cell at low temperatures, as shown in Figure S17a (Supporting Information), the cell using 1T-Li_xMoS_2/HC_3N_4/PP can still realize effective reversible cycling at −10 °C. Moreover, the capacity contribution attributed to 1T-Li_xMoS_2/HC_3N_4 can still be observed in the corresponding GCD curve (Figure S17b, Supporting Information). The above results confirm that the catalytic mechanism of "electron-Li^+" reservoirs is still feasible at low temperatures. High areal capacity is also an important goal for commercial LSBs.[26] As shown in Figure 4g, the cell with 1T-Li_xMoS_2/HC_3N_4/PP reaches an initial areal capacity close to 6 mAh cm^{-2} at a high sulfur loading of 5 mg cm^{-2} and the cycling capability lasts for 100 cycles with the areal capacity of ≈4 mAh cm^{-2}. Further, the sulfur loading was further increased to 7.5 mg cm^{-2} with an E/S ratio of only 6.8 μL mg^{-1}. The test results showed that the modified cell achieved an initial areal capacity of 7.1 mAh cm^{-2} at 0.1C, which meets the requirements for commercial batteries (Figure S18, Supporting Information). The potential performance of 1T-Li_xMoS_2/HC_3N_4/PP under high sulfur loading is demonstrated by comparing the performance metrics (sulfur loading, sulfur content, initial capacity, final capacity, number of cycle laps, and areal capacity) with recent work (Figure 4h).[27] The above tests demonstrate that 1T-Li_xMoS_2/HC_3N_4/PP can help LSBs achieve excellent cycling performance under various conditions, which provides an important reference for the commercial application of LSBs.

2.5. Analysis of Polysulfide Shuttling Inhibition via Fast Conversion Kinetics

In order to further investigate the modification mechanism and electrocatalytic ability of 1T-Li_xMoS_2/HC_3N_4, the in situ UV and

ToF-SIMS tests were performed. The in situ UV allows the observation of concentration changes with different sulfur species during the process in the cell. The higher concentrations of $S_3^{\cdot-}$ and S_8^{2-}[25b,28] and extended discharge time are observed in 1T-Li_xMoS_2/HC_3N_4 than in HC_3N_4 (**Figure** 5a,b). This phenomenon can be attributed to the ability of 1T-Li_xMoS_2/HC_3N_4 to promote the formation of $S_3^{\cdot-}$, propelling the ring-opening reaction of the S_8 molecule and resulting in higher sulfur utilization.[29] The distribution of sulfur species in the cathode and anode after cycling was further constructed obviously by TOF-SIMS, providing a visual analysis of sulfur utilization. Notably, the cathode of the cell with 1T-Li_xMoS_2/HC_3N_4/PP exhibits stronger intensity of secondary S^- ions (Figure 5c). Similarly, in the ToF-SIMS surface profiles, 1T-Li_xMoS_2/HC_3N_4/PP system has a larger and uniform area of the S^- regions, representing higher sulfur utilization (Figure 5d). Further, the severe shuttle effect leads to the appearance of "dead sulfur species" dominated by Li_2S on the surface of the Li anode. The 3D constructure images of Li anode show a fewer and shallower distribution of Li_2S with 1T-Li_xMoS_2/HC_3N_4/PP, and the smaller area of the Li_2S^- regions in the 1T-Li_xMoS_2/HC_3N_4/PP system is due to the enhanced kinetics for SRRs, which prevents the shuttle effect (Figure 5e,f). The above analysis further reveals the modification mechanism of 1T-Li_xMoS_2/HC_3N_4 and confirms the excellent electrocatalytic ability for LSBs.

3. Conclusion

In this work, a catalytic strategy is proposed for "electron-Li^+" reservoirs by reconstructing the phase of electrochemical catalyst based on the mechanism that Li^+ regulates the conversion kinetics of sulfur species. The 1T-Li_xMoS_2 severs as an auxiliary "Li^+ source" for fast Li^+ transport and the HC_3N_4 acts as an electron-donor for electronic structure regulation, which synergistically accelerates the redox kinetics for sulfur. From the DFT calculations, electrochemical analysis and TOF-SIMS, the kinetic modulation mechanism is investigated, confirming the excellent electrochemical catalysis of 1T-Li_xMoS_2/HC_3N_4. As a result, the 1T-Li_xMoS_2/HC_3N_4 achieves an initial discharge specific capacity of 1668 mAh g^{-1} at 0.1C, maintains high-capacity retention of 76.2%/90.4% after 100 cycles at high (60 °C)/low (0 °C) temperatures, respectively. Impressively, an initial areal capacity of 6 mAh cm^{-2} is also achieved even at a high sulfur loading of 5 mg cm^{-2}. This work presents the precise regulations of SRRs and SORs from a new perspective, and points out the way for further optimization of LSBs electrocatalysts toward high/low- temperature surroundings.

Supporting Information

Supporting Information is available from the Wiley Online Library or from the author.

Acknowledgements

The authors acknowledge support from the National Natural Science Foundation of China (Nos. 22109135, 52172242, and 52273306), Hunan Provincial Natural Scientific Foundation of China (Nos. 2022JJ40423, 2023JJ50239, 2023JJ30575, and 2024JJ2050), China Postdoctoral Science Foundation (No. 2022TQ0265), Natural Science Foundation of Jiangsu Province (BK 20210130), Scientific Research Fund of Hunan Provincial Education Department (Nos. 23B0126, 22C0056, and 22A0116), the Opening funding from Key Laboratory of Engineering Dielectrics and Its Application (Harbin University of Science and Technology) (No. KFM202507, Ministry of Education). Dr. J. Wang also acknowledges the financial support by the Alexander von Humboldt Foundation and the basic funding of the Helmholtz Association, and the technical support from Nano-X, Suzhou Institute of Nano-Tech and Nano-Bionics, Chinese Academy of Sciences (SINANO-CAS).

Conflict of Interest

The authors declare no conflict of interest.

Data Availability Statement

The data that support the findings of this study are available from the corresponding author upon reasonable request.

Keywords

electron-Li^+ transport, lithium-sulfur battery, phase reconstruction, sulfur oxidation reaction, sulfur reduction reaction

Received: June 21, 2024
Revised: October 19, 2024
Published online: November 9, 2024

[1] a) C. Zhang, Y. Yang, X. Liu, M. Mao, K. Li, Q. Li, G. Zhang, C. Wang, *The Innovation* **2023**, *4*, 100518; b) B. Sun, Z. Sun, Y. Yang, X. L. Huang, S. C. Jun, C. Zhao, J. Xue, S. Liu, H. K. Liu, S. X. Dou, *ACS Nano* **2024**, *18*, 28; c) F. Ye, Z. Wang, M. Li, J. Zhang, D. Wang, M. Liu, A. Liu, H. Lin, H.-T. Kim, J. Wang, *Nano Lett.* **2024**, *24*, 6850.
[2] Y. Chen, T. Wang, H. Tian, D. Su, Q. Zhang, G. Wang, *Adv. Mater.* **2021**, *33*, 2003666.
[3] a) Z. Wang, Y. Yan, Y. Zhang, Y. Chen, X. Peng, X. Wang, W. Zhao, C. Qin, Q. Liu, X. Liu, Z. Chen, *Carbon Energy* **2023**, *5*, e306; b) Z. Yang, Z. Guo, X. Wang, W. Lu, Q. Wang, Y. Zhao, M. Yao, P. Gao, D. Zhang, F. Du, *Energy Storage Mater.* **2024**, *67*, 103276; c) S. Liu, X. Liu, M. Chen, D. Wang, X. Ge, W. Zhang, X. Wang, C. Wang, T. Qin, H. Qin, L. Qiao, D. Zhang, X. Ou, W. Zheng, *Nano Res.* **2022**, *15*, 7199.
[4] a) M. Zhao, X. Chen, X.-Y. Li, B.-Q. Li, J.-Q. Huang, *Adv. Mater.* **2021**, *33*, 2170100; b) R. Guo, Y. Yang, C. Zhao, F. Huo, J. Xue, J. He, B. Sun, Z. Sun, H. K. Liu, S. X. Dou, *Adv. Funct. Mater.* **2024**, *34*, 2313168.
[5] L. Ma, Y. Wang, Z. Wang, J. Wang, Y. Cheng, J. Wu, B. Peng, J. Xu, W. Zhang, Z. Jin, *ACS Nano* **2023**, *17*, 11527.
[6] a) J. Wang, G. Li, D. Luo, Y. Zhang, Y. Zhao, G. Zhou, L. Shui, X. Wang, Z. Chen, *Adv. Energy Mater.* **2020**, *10*, 2002076; b) C. Zhao, F. Huo, Y. Yang, J. Ruan, F. Chai, H. Xu, Y. Liu, L. Zhang, A. Cabot, Z. Sun, Y. Zhang, *Adv. Funct. Mater.* **2024**, *34*, 2402175.
[7] a) Q. Sheng, H. Liu, Y. Liu, B. Jin, M. Cui, Y. Li, N. Gao, X. Lang, Q. Jiang, *Chem. Eng. J.* **2023**, *476*, 146880; b) R. Paste, S. Li, J.-H. Fu, Y.-H. Chiang, A. I. Inamdar, M.-H. Chiang, V. Tung, H.-C. Lin, C. W. Chu, *J. Mater. Chem. A* **2023**, *11*, 8265; c) V. P. Nguyen, J. S. Park, H. C. Shim, J. M. Yuk, J.-H. Kim, D. Kim, S.-M. Lee, *Adv. Funct. Mater.* **2023**, *33*, 2303503; d) C. Zhang, B. Fei, D. Yang, H. Zhan, J. Wang, J. Diao, J. Li, G. Henkelman, D. Cai, J. J. Biendicho, J. R. Morante, A. Cabot, *Adv. Funct. Mater.* **2022**, *32*, 2201322.

[8] Y. Zhang, Z. Mu, C. Yang, Z. Xu, S. Zhang, X. Zhang, Y. Li, J. Lai, Z. Sun, Y. Yang, Y. Chao, C. Li, X. Ge, W. Yang, S. Guo, *Adv. Funct. Mater.* **2018**, *28*, 1707578.
[9] M. Li, Z. Zhou, L. Hu, S. Wang, Y. Zhou, R. Zhu, X. Chu, A. Vinu, T. Wan, C. Cazorla, J. Yi, D. Chu, *ACS Appl. Mater. Interfaces* **2022**, *14*, 16338.
[10] a) M. Jin, G. Sun, Y. Wang, J. Yuan, H. Zhao, G. Wang, J. Zhou, E. Xie, X. Pan, *ACS Nano* **2024**, *18*, 2017; b) Z. Li, I. Sami, J. Yang, J. Li, R. V. Kumar, M. Chhowalla, *Nat. Energy* **2023**, *8*, 84.
[11] a) Y. Cao, C. Liu, M. Wang, H. Yang, S. Liu, H. Wang, Z. Yang, F. Pan, Z. Jiang, J. Sun, *Energy Storage Mater.* **2020**, *29*, 207; b) R. Guo, Y. Yang, X. L. Huang, C. Zhao, B. Hu, F. Huo, H. K. Liu, B. Sun, Z. Sun, S. X. Dou, *Adv. Funct. Mater.* **2024**, *34*, 2307108; c) J. Wang, J. Zhang, Y. Zhang, H. Li, P. Chen, C. You, M. Liu, H. Lin, S. Passerini, *Adv. Mater.* **2024**, *36*, 2402792.
[12] a) X. Wu, R. Xie, D. Cai, B. Fei, C. Zhang, Q. Chen, B. Sa, H. Zhan, *Adv. Funct. Mater.* **2024**, *34*, 2315012; b) J. Wang, L. Jia, H. Liu, C. Wang, J. Zhong, Q. Xiao, J. Yang, S. Duan, K. Feng, N. Liu, W. Duan, H. Lin, Y. Zhang, *ACS Appl. Mater. Interfaces* **2020**, *12*, 12727; c) J. Zhang, R. He, Q. Zhuang, X. Ma, C. You, Q. Hao, L. Li, S. Cheng, L. Lei, B. Deng, X. Li, H. Lin, J. Wang, *Adv. Sci.* **2022**, *9*, 2202244.
[13] a) D. Yang, C. Li, M. Sharma, M. Li, J. Wang, J. Wei, K. Liu, Y. Zhang, J. Li, G. Henkelman, Q. Zhang, A. Cabot, *Energy Storage Mater.* **2024**, *66*, 103240; b) J. Wang, L. Jia, J. Zhong, Q. Xiao, C. Wang, K. Zang, H. Liu, H. Zheng, J. Luo, J. Yang, H. Fan, W. Duan, Y. Wu, H. Lin, Y. Zhang, *Energy Storage Mater.* **2019**, *18*, 246.
[14] a) L. Li, H. Tu, J. Wang, M. Wang, W. Li, X. Li, F. Ye, Q. Guan, F. Zhu, Y. Zhang, Y. Hu, C. Yan, H. Lin, M. Liu, *Adv. Funct. Mater.* **2023**, *33*, 2212499; b) J. Wang, H. Liu, J. Zhang, Q. Xiao, C. Wang, Y. Zhang, M. Liu, Q. Kang, L. Jia, D. Wang, Q. Li, W. Duan, H. Adenusi, S. Passerini, Y. Zhang, H. Lin, *Energy Storage Mater.* **2024**, *67*, 103289.
[15] a) X. Chen, Z. Chen, J. Li, *Chin. Sci. Bull.* **2013**, *58*, 1632; b) S. Park, C. Kim, S. O. Park, N. K. Oh, U. Kim, J. Lee, J. Seo, Y. Yang, H. Y. Lim, S. K. Kwak, G. Kim, H. Park, *Adv. Mater.* **2020**, *32*, 2001889.
[16] M. Chen, W. Xu, S. Jamil, S. Jiang, C. Huang, X. Wang, Y. Wang, H. Shu, K. Xiang, P. Zeng, *Small* **2018**, *14*, 1803134.
[17] M. Chen, N. Wang, W. Zhou, X. Zhu, Q. Wu, M.-H. Lee, D. Zhao, S. Ning, M. An, L. Li, *Small* **2023**, *19*, 2303015.
[18] L. Liu, J. Wu, L. Wu, M. Ye, X. Liu, Q. Wang, S. Hou, P. Lu, L. Sun, J. Zheng, L. Xing, L. Gu, X. Jiang, L. Xie, L. Jiao, *Nat. Mater.* **2018**, *17*, 1108.
[19] Y. C. Jeong, J. H. Kim, S. H. Kwon, J. Y. Oh, J. Park, Y. Jung, S. G. Lee, S. J. Yang, C. R. Park, *J. Mater. Chem. A* **2017**, *5*, 23909.
[20] M. Tiwari, A. Singh, D. Thakur, S. K. Pattanayek, *Carbon* **2022**, *197*, 311.
[21] J. Chen, W. R. Walker, L. Xu, O. Krysiak, Z. She, M. A. Pope, *ACS Nano* **2020**, *14*, 5636.
[22] a) J. Liu, H. Zhao, J. Xia, L. Yi, X. Chen, D. Li, S. Ni, X. Su, Y. Chen, M. Liu, X. Wang, *J. Energy Chem.* **2024**, *94*, 758; b) Z. Zhang, X. Liu, D. Wang, H. Qin, X. He, B. Gao, G. Li, W. Zheng, Z. Zhuang, G. Yang, X. Ou, *Energy Storage Mater.* **2024**, *69*, 103419.
[23] R. Soni, J. B. Robinson, P. R. Shearing, D. J. L. Brett, A. J. E. Rettie, T. S. Miller, *Energy Storage Mater.* **2022**, *51*, 97.
[24] a) T. Sun, X. Zhao, B. Li, H. Shu, L. Luo, W. Xia, M. Chen, P. Zeng, X. Yang, P. Gao, Y. Pei, X. Wang, *Adv. Funct. Mater.* **2021**, *31*, 2101285; b) Y. Luo, D. Zhang, Y. He, W. Zhang, S. Liu, K. Zhu, L. Huang, Y. Yang, G. Wang, R. Yu, H. Shu, X. Wang, M. Chen, *Chem. Eng. J.* **2023**, *474*, 145751.
[25] a) S. Tian, G. Liu, S. Xu, C. Han, K. Tao, J. Huang, S. Peng, *Adv. Funct. Mater.* **2023**, *34*, 2309437; b) D. Zhang, T. Duan, Y. Luo, S. Liu, W. Zhang, Y. He, K. Zhu, L. Huang, Y. Yang, R. Yu, X. Yang, H. Shu, Y. Pei, X. Wang, M. Chen, *Adv. Funct. Mater.* **2023**, *33*, 2306578.
[26] T. Wang, J. He, X.-B. Cheng, J. Zhu, B. Lu, Y. Wu, *ACS Energy Lett.* **2023**, *8*, 116.
[27] a) X. Ao, Y. Kong, S. Zhao, Z. Chen, Y. Li, X. Liao, B. Tian, *Angew. Chem., Int. Ed.* **2024**, https://doi.org/10.1002/anie.202415036; b) H. Song, T. T. Nguyen, R. Chu, Y. Bai, N. H. Kim, J. H. Lee, *Nano Energy* **2024**, *128*, 109859; c) X. Zuo, L. Wang, M. Zhen, T. You, D. Liu, Y. Zhang, *Angew. Chem., Int. Ed.* **2024**, *63*, 202408026; d) X. Wang, L. Chen, Y. Yu, W. Wang, L. Yue, Z. Shao, H. Wu, Y. Li, *Adv. Funct. Mater.* **2024**, *34*, 2406290; e) H. Zhang, M. Zhang, R. Liu, T. He, L. Xiang, X. Wu, Z. Piao, Y. Jia, C. Zhang, H. Li, F. Xu, G. Zhou, Y. Mai, *Nat. Commun.* **2024**, *15*, 5451; f) F. Cao, X. Zhang, Z. Jin, J. Zhang, Z. Tian, D. Kong, Y. Li, Y. Li, L. Zhi, *Adv. Energy Mater.* **2024**, *14*, 2303893; g) A. Coskun, M. Liu, Z. Wu, S. Liu, T. Guo, P. Chen, X. Cao, S. Pan, T. Zhou, L. Pompizii, M. Najafov, Y. Fu, *Angew. Chem., Int. Ed.* **2024**, https://doi.org/10.1002/anie.202417624; h) L.-L. Su, N. Yao, Z. Li, C.-X. Bi, Z.-X. Chen, X. Chen, B.-Q. Li, X.-Q. Zhang, J.-Q. Huang, *Angew. Chem., Int. Ed.* **2024**, *63*, 202318785; i) R. Yan, Z. Zhao, R. Zhu, M. Wu, X. Liu, M. Adeli, B. Yin, C. Cheng, S. Li, *Angew. Chem., Int. Ed.* **2024**, *63*, 202404019; j) Q. Yang, J. Cai, G. Li, R. Gao, Z. Han, J. Han, D. Liu, L. Song, Z. Shi, D. Wang, G. Wang, W. Zheng, G. Zhou, Y. Song, *Nat. Commun.* **2024**, *15*, 3231.
[28] W. Zhang, M. Chen, Y. Luo, Y. He, S. Liu, Y. Ye, M. Wang, Y. Chen, K. Zhu, H. Shu, M. Liu, J. Hou, T. Duan, X. Wang, *Chem. Eng. J.* **2024**, *486*, 150411.
[29] P. Zeng, X. Zhou, J. Peng, X. Huang, B. Chang, G. Chen, M. Chen, L. Zheng, Y. Pei, J. Su, X. Wang, *Adv. Funct. Mater.* **2023**, *33*, 2211818.